

Microbial interactions in the anaerobic oxidation of methane: Model simulations constrained by process rates and activity patterns

He, Xiaojia,^{1,*} Chadwick, Grayson,² Kempes, Christopher,⁴ Shi, Yimeng,^{1,#} McGlynn, Shawn^{2,3}, Orphan, Victoria,² and Meile, Christof¹

¹ Department of Marine Sciences, University of Georgia, Athens, GA, USA

² Division of Geological and Planetary Sciences, California Institute of Technology, Pasadena, CA, USA

³ Earth-Life Science Institute, Tokyo Institute of Technology, Ookayama, Meguro-ku, Tokyo, Japan

⁴ Santa Fe Institute, Santa Fe, NM, USA

Department of Statistics and Biostatistics, Rutgers University, New Brunswick, NJ, USA

*Corresponding author

xiaojia.he25@uga.edu

Department of Marine Sciences

University of Georgia

Athens GA 30602

USA

For submission to: Environmental Microbiology

Running title: **Process modeling of anaerobic methane oxidation**

This article has been accepted for publication and undergone full peer review but has not been through the copyediting, typesetting, pagination and proofreading process, which may lead to differences between this version and the Version of Record. Please cite this article as doi: 10.1111/1462-2920.14507

Originality-Significance Statement

We present a three-dimensional numerical model combining reaction kinetics and energetics to explore potential microbial interactions underlying anaerobic oxidation of methane (AOM) in archaeal-bacterial consortia. We compare model simulations to measurement-derived cell-specific AOM rates and observed intra-aggregate activity patterns. This integration of data from both the micro- and the macro-scale provides significant constraints on the parameterization of reaction kinetics. Model simulations assess the feasibility and constraints on diffusive exchange of solutes, and confirm conductive electron transport, recently proposed based on genomic data and microscopy, as one potentially viable syntrophic mechanism, while ruling out some models relying on diffusive exchange of chemical intermediates.

Summary

Proposed syntrophic interactions between the archaeal and bacterial cells mediating anaerobic oxidation of methane coupled with sulfate reduction include electron transfer through (1) the exchange of H_2 or small organic molecules between methane-oxidizing archaea and sulfate-reducing bacteria, (2) the delivery of disulfide from methane-oxidizing archaea to bacteria for disproportionation, and (3) direct interspecies electron transfer. Each of these mechanisms was implemented in a reactive transport model. The simulated activities across different arrangements of archaeal and bacterial cells and aggregate sizes were compared to empirical data for AOM rates and intra-aggregate spatial patterns of cell-specific anabolic activity determined by FISH-nanoSIMS. Simulation results showed that rates for chemical diffusion by mechanism (1) were limited by the build-up of metabolites, while mechanisms (2) and (3) yielded cell specific rates and archaeal activity distributions that were consistent with observations from single cell resolved FISH-nanoSIMS analyses. The novel integration of both intra-aggregate and environmental data provided powerful constraints on the model results, but the similarities in model outcomes for mechanisms (2) and (3) highlight the need for additional observational data (e.g. genomic or physiological) on electron transfer and metabolic functioning of these globally important methanotrophic consortia.

1. Introduction

Anaerobic oxidation of methane (AOM) describes the conversion of methane to CO₂ in the absence of oxygen, and in marine sediments is primarily coupled to the reduction of sulfate, following the general reaction:



Hinrichs et al. (1999) first identified groups of uncultured archaea hypothesized to be involved in anaerobic oxidation of methane from deep-sea methane seeps using archaeal 16S rRNA diversity surveys and stable isotope analysis of archaeal lipids. Subsequently anaerobic methanotrophic archaea (ANME) were visualized in sediments and shown to form multi-celled aggregations with deltaproteobacteria bacteria, spanning from micron-scale aggregates to mats covering meter-scale reef-like structures (Boetius et al. 2000, Orphan et al. 2001, Orphan et al. 2002, Michaelis et al. 2002). Since then, our understanding of the diversity of ANME archaea and bacteria involved in this process has expanded along with a growing list of terminal electron acceptors coupled to methane oxidation, including nitrate (Haroon et al. 2013, Raghoebarsing et al. 2006); iron and manganese (Beal et al. 2009, Ettwig et al. 2016, Barr-Or et al. 2017); and humic acid analogs (Scheller et al. 2016).

AOM in marine sediments is estimated to consume about 382 Tgyr⁻¹ of methane, which is about three-quarters of the global net methane emission to the atmosphere (Reeburgh 2007). AOM thus acts as a significant sink for methane, a greenhouse gas with a warming potential 25 times that of CO₂ over 100 years (Forster et al. 2007). However, the details of the physiological mechanism underlying AOM are still not completely understood, and it is possible multiple mechanisms are used depending on the specific microorganisms and environments (e.g., Alperin and Hoehler 2010, Timmers et al. 2017, McGlynn 2017). For microbial consortia consisting of archaea and bacteria, classical syntrophic electron transfer through the exchange of solutes (mediated interspecies electron transfer, MIET) was proposed early on, where H₂, formate, acetate, methanol and methylsulfides have been considered as intermediates that diffuse from methane-oxidizing archaea to sulfate-reducing bacteria (SRB-MIET; Reeburgh 1976, Hoehler et al., 1998, Valentine et al. 2000 Sørensen et al. 2001, Moran et al. 2008, Orcutt and Meile 2008). Alternatively, Milucka et al. (2012) proposed the exchange of disulfide, produced by ANME archaea coupling methane oxidation to sulfate reduction directly, and consumed by associated sulfur disproportionating bacteria (HS₂-MIET). More recently, direct interspecies electron transfer (DIET) has been hypothesized as a principal mechanism responsible for electron transfer in ANME-SRB consortia (McGlynn et al. 2015, Wegener et al. 2015). It has been shown that methane-oxidation by ANME-2 archaea in deep-sea sediments can be catabolically and anabolically decoupled from sulfate-reduction and the activity of their deltaproteobacterial partners using soluble oxidants, including anthraquinone-2,6-disulfonate (AQDS), humic acids, and iron(III)-citrate (Scheller et al. 2016), consistent with a syntrophic electron exchange between Archaea and Bacteria in the consortia (McGlynn et al. 2015, Wegener et al. 2015). Moreover, large S-layer associated multi-heme cytochromes were observed to be encoded by ANME-2 genomes, and appear to be related to electron transfer in ANME-2/SRB consortia as observed by transmission electron

microscopy (TEM) (McGlynn et al. 2015, Krukenberg et al. 2018). TEM on thin sections of thermophilic AOM consortia further reported pili-like structures with diameters of 10 nm and apparent lengths of 100 nm to >1000 nm, which connect SRB HotSeep-1 and ANME-1 cells (Wegener et al. 2015), suggestive of DIET.

In this study, we simulate the activity of AOM in microbial consortia for mediated interspecies electron transfer, in which the bacteria reduce sulfate, disproportionate disulfide, or participate in direct electron transfer (Figure 1). Earlier efforts by McGlynn et al. (2015) employed an idealized set of models to compare the physical and physiological processes and consequences of direct electron exchange to a diffusive intermediate for syntrophic aggregates. This generalized approach suggested that at measured AOM rates, chemical diffusivities can result in strong gradients of cellular activity in multi-celled syntrophic aggregates, which is inconsistent with single-cell activity measurements from stable-isotope incorporation studies using fluorescence *in situ* hybridization coupled with nanoscale secondary ion mass spectrometry (FISH-nanoSIMS; McGlynn et al. 2015). The importance of efficient exchange mechanisms between microbial partners can be illustrated by considering the spatial variation in substrate concentrations within an active microbial consortium. Consider an aggregate of several μm radius, in which sulfate-reducing bacteria surround an inner sphere of methane-oxidizing archaea. Assuming a constant, typical rate of substrate consumption on the order of $5 \text{ fmol cell}^{-1} \text{ d}^{-1}$, and transport by chemical diffusion, substrate concentrations can vary substantially across the aggregate. In contrast, faster conductive transport yields almost uniform substrate levels, and presumably, microbial activity, across the aggregate (see Supporting Information Appendix A3). This simple calculation illustrates the fundamental difference between MIET and DIET mechanisms, but it lacks feedbacks of local environmental conditions (e.g. chemical concentrations, pH, etc.) on microbial activity.

Recent numerical modeling has shown the feasibility of direct electron transfer in single-cell pairs (Storck et al. 2016) and microbial biofilms (Kroth et al. 2015, Strycharz-Glaven et al. 2011). However, modeling efforts have not yet been applied to characterize the direct extracellular electron transfer behavior between methane-oxidizing ANME archaea and its sulfate-reducing bacterial partner with feedbacks of local environmental conditions. Here, we build on the previous modeling efforts by Orcutt and Meile (2008), Alperin and Hoehler (2009), and McGlynn et al. (2015), to evaluate the various hypotheses regarding the potential mechanisms of AOM within these uncultured archaeal-bacterial consortia. We compare the modeled methane oxidation rates and activity distribution patterns to observational data from methane seeps at Hydrate Ridge off the coast of Oregon, USA, and explore the effect of consortia size, the intra-aggregate spatial distribution of archaeal and bacterial cells, and pH variations. This allows for direct comparison of the different mechanisms. By assessing the sensitivity of model outputs towards poorly constrained model parameters (e.g. rate constants), in conjunction with comparison to data at both the macro and the micro scales, it is further possible to constrain model parameters for use in larger scale models.

2. Modeling Procedure

The model domain included a single spherical microbial aggregate. Several different spatial distributions of archaea and bacteria within an aggregate were investigated (Fig. S1), reflecting distribution patterns observed in nature (see e.g. Fig 1a in McGlynn et al. 2015). Cell volumes assigned to archaea and bacteria were based on observed cell numbers and sizes reported (Knittel et al. 2005, Aoki et al. 2014, Boetius et al. 2000). Cell radii were set to 0.4 μm for both archaea and bacteria, with a 1 archaea : 1 bacteria cell ratio.

2.1. Governing equations

The governing equations simulating the reaction and transport processes are of the form:

$$\frac{\partial \phi C_i}{\partial t} = \phi \mathbf{R}_i + \nabla \cdot (\phi \mathbf{D}_i \nabla C_i), \quad \text{Eq (1)}$$

where ϕ is the porosity and C_i is the concentration of chemical species i . \mathbf{D}_i represents the in situ diffusion coefficient, adjusted for tortuosity and EPS as in Orcutt and Meile (2008), and \mathbf{R}_i is the net reaction rate.

The rate of a metabolic reaction X is expressed as (Jin and Bethke 2003, Jin and Bethke 2007)

$$R^X = F_k^X F_T^X, \quad \text{Eq (2)}$$

where F_k^X represents the reaction kinetics. It is implemented as the product of a cell-specific rate constant k , the cell density B (cells per volume), and the abundance of substrate S using a Monod expression with half-saturation constant K_m^S :

$$F_k^X = kB \frac{S}{K_m^S + S} \quad \text{Eq (3)}$$

The thermodynamic factor ($0 \leq F_T^X \leq 1$) reflects that there must be sufficient free energy available from the reactions to fuel ATP synthesis and cell maintenance, which is given by

$$F_T^X = \max \left(0, 1 - \exp \left(-\frac{f_X}{\chi R_{gas} T} \right) \right), \quad \text{Eq (4)}$$

where χ , the number of ATP synthesized per reaction, is set to 1 (Orcutt and Meile 2008), R_{gas} is the universal gas constant ($8.314 \text{ J K}^{-1} \text{ mol}^{-1}$) and T is temperature (281.15 K). f_X represents the thermodynamic driving force, relating the free energy yield of that reaction to the energy required to synthesize ATP (Jin and Bethke 2003, Jin and Bethke 2007), which is expressed as:

$$f_X = -\Delta G_X - \Delta G_{ATP}, \quad \text{Eq (5)}$$

where ΔG_{ATP} represents a minimum energy required for ATP synthesis. Tran and Uden (1998) demonstrated ADP phosphorylation proceeded at energies as low as 42 kJ mol^{-1} . With a H^+/ATP ratio of 4 (Pänke and Rumberg 1997) and $\Delta G_{\text{ADP} \rightarrow \text{ATP}} = +42 \text{ kJ mol}^{-1}$, this results in ΔG_{ATP} on the order of $10 \text{ kJ mol}^{-1} \text{ H}^+$ (Hoehler et al. 2001; note that this minimum energy requirement of 10 instead of 1 kJ mol^{-1} used in Orcutt and Meile (2008) leads to maximum rates slightly lower than the one reported there).

The Gibbs free energy of the reaction is computed as:

$$\Delta G_X = \Delta G_X^0 + R_{gas}T \ln Q_X \quad \text{Eq (6)}$$

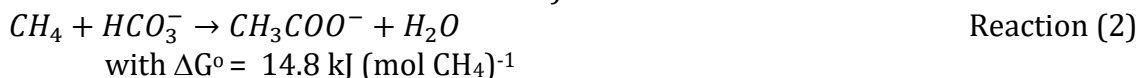
with the reaction quotient $Q = \prod a_i^{v_j}$, where v are stoichiometric coefficients and a denote activities, computed as the product of concentrations and activity coefficients as given in Orcutt and Meile (2008).

Acid-base reactions of the DIC and borate system were accounted for using the kinetic formalism given in Zeebe and Wolf-Gladrow (2005). To account for protonation/deprotonation on cell surfaces, surface site concentrations of $1 \mu\text{mol (mg dry cell)}^{-1}$ carboxy and $1 \mu\text{mol (mg dry cell)}^{-1}$ amino groups were considered (Konhauser 2006), with an aggregate biomass of $0.12 \text{ (mg dry cell) m}^{-3}$ (Boetius et al. 2000). Kinetic constants were taken from the literature (Kaplan et al. 1971, Wallerstein et al. 2015), consistent with equilibrium constants given in Phoenix et al. (2002) and Burgess et al. (2006) and microscopic reversibility. See Supporting Information Appendix A5 for a detailed description.

Three different mechanisms for the interaction between archaea and bacteria were implemented (Fig. 1), as described below. In the absence of known intermediates, we considered acetate and H_2 (not shown) as representative dissolved intermediates in MIET; for DIET, we assumed that electrons from the oxidation of methane are captured by an electron acceptor (D) from which they are transferred onto a redox-active molecule (reduced: MH; oxidized: M) located on conductive pili, embedded in a matrix of extracellular polymeric substances (EPS), or transferred by dissolved electron carriers through diffusive transport processes. We did not differentiate between conductive pili or a conductive matrix in this study, but note that microbes have been shown to utilize pili-like structures (Wegener et al. 2015; Reguera et al., 2005, 2006; El-Naggar et al., 2008), extracellular biofilm matrix (Viridis et al. 2016; Ordóñez et al. 2016), and multi-heme cytochromes (McGlynn et al. 2015) for extracellular electron transport.

2.1.1. Mediated interspecies electron transfer

Methane is oxidized by the archaea, with the product, here acetate (Ac), serving as an electron donor for sulfate reducing bacteria (for reactions with H_2 as intermediate see Orcutt and Meile 2008):



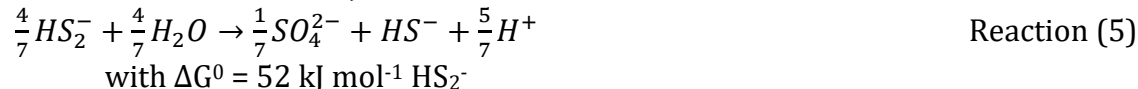
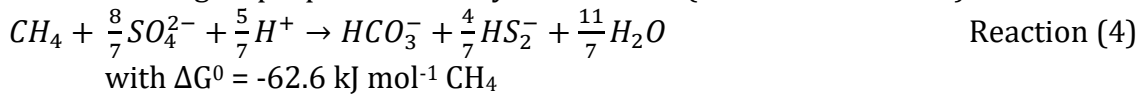
The kinetic factors are (see justification for multiple limiting substrate Monod kinetics in Beyenal et al. 2003; Cherif and Loreau 2010; Gonzo et al. 2014; Zinn et al. 2004):

$$F_k^{R2} = k_A B_A \frac{\text{CH}_4}{K_m^{\text{CH}_4} + \text{CH}_4} \quad \text{Eq (7)}$$

$$F_k^{R3} = k_B B_B \frac{\text{SO}_4^{2-}}{K_m^{\text{SO}_4} + \text{SO}_4^{2-}} \frac{\text{Ac}}{K_m^{\text{Ac}} + \text{Ac}} \quad \text{Eq (8)}$$

2.1.2. Disulfide pathway

In the disulfide pathway, the archaea oxidize methane and reduce sulfate, with disulfide being disproportionated by the bacteria (Milucka et al. 2012):



The kinetic factors are

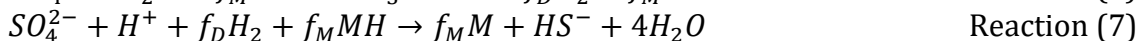
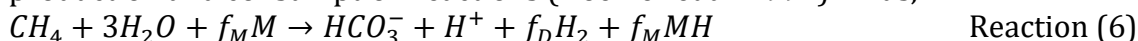
$$F_k^{R4} = k_A B_A \frac{CH_4}{K_m^{CH_4} + CH_4} \frac{SO_4^{2-}}{K_m^{SO_4} + SO_4^{2-}} \quad \text{Eq (9)}$$

$$F_k^{R5} = k_B B_B HS_2^- \quad \text{Eq (10)}$$

2.1.3. Direct interspecies electron transfer

The archaea are considered responsible for methane oxidation and the bacteria for the reduction of sulfate. Direct electron transfer involves the loading of electrons from a primary electron acceptor (D) onto a redox-active molecule (e.g. cytochromes; reduced form: MH; oxidized form: M) located on conductive pili or matrix, the transfer from the archaea to the bacteria, and the offloading and use of electrons in sulfate reduction. The D molecule and its reduced form DH act as an 'electron pool' to temporally store electrons produced from methane oxidation. Electrons are then moved from the archaea to the bacteria either via a DIET mechanism, or may be transferred onto solutes that are subject to diffusive exchange.

H₂ was modeled as the electron pool molecule (DH) in our models. This is highly idealized; it was chosen to minimize the level of model complexity in the light of our lack of knowledge on the actual mechanism, and because H₂, with its fast turnover time, has been shown to be an important indicator for the energetics of methane production and consumption reactions (Hoehler et al. 1994). Thus,



where 8 electrons released in the oxidation of methane to CO₂ result in $f_M \in [0,8]$ with $f_D = (8-f_M)/2$, and the thermodynamic factor (Eq. 4) was calculated accordingly (see Supplementary Information Appendix A4). The default values for f_M and f_D in this study were 7.2 and 0.4, respectively. The values for f_M and f_D were varied in Fig. 5C for sensitivity analysis. The kinetic factors are

$$F_k^{R6} = k_A B_A \frac{CH_4}{K_m^{CH_4} + CH_4} M \quad \text{Eq (11)}$$

$$F_k^{R7} = k_B B_B \frac{SO_4^{2-}}{K_m^{SO_4} + SO_4^{2-}} MH \quad \text{Eq (12)}$$

There is an ongoing debate over whether electrons transfer along the conductive pili/biofilms proceeds via electron superexchange (i.e. electron hopping; Strycharz-Glaven et al. 2011, 2012) or metallic-like conductivity (Malvankar et al. 2011, 2012). Electron superexchange recently proposed by Strycharz-Glaven et al. (2011) is

based on the abundance and prevalent role of multiple redox molecules located on conductive cell outer membranes, pili, or extracellular matrices (Strycharz-Glaven et al. 2012). We modeled the direct electron transport via conjugated redox-active molecules building on recent evidence of the presence and expression of large multi-heme cytochrome genes in ANME-1 (Meyerdierks et al. 2010; Kletzin et al. 2015) and ANME-2 (McGlynn et al. 2015; Kletzin et al. 2015) genomes. It is described as (Strycharz-Glaven et al. 2011):

$$J_{(x)} = k_f M H_{(x)} M_{(x+\delta)} - k_b M_{(x)} M H_{(x+\delta)} \quad \text{Eq (13)}$$

where J is the electron flux in mol e⁻ m⁻² s⁻¹, x is the location along the filament, δ is the distance between two redox molecules and k_f and k_b are forward and backward rate constants.

2.1.3.1. Gradient-driven DIET

In the case of concentration gradient-driven electron transport, the forward and backward electron transport rate constants are equal, $k_f = k_b = k^0$, and the flux can be simplified into a diffusion-like expression:

$$J_{G,(x)} = -D_{MH} \left(\frac{\partial MH}{\partial x} \right), \quad \text{Eq (14)}$$

where $D_{MH} = k^0 M_{tot} \delta$ is the effective diffusion coefficient (see Strycharz-Glaven et al. 2011 for a derivation), where M_{tot} is the total concentration (=M+MH). Thus, the governing equation for MH can be expressed as:

$$\phi \frac{\partial MH}{\partial t} = \nabla \cdot (\phi D_{MH} \nabla MH) + R_r \quad \text{Eq (15)}$$

where D_{MH} is set to a constant value within the aggregate (see above) and 0 outside and R_r is the net production rate.

2.1.3.2. Electric field-driven DIET

In the presence of an electric field, forward and backward electron transport rate constants differ and the current conducted can be expressed as

$$J_{EF} = k^0 M \cdot MH \left(e^{\frac{nF(\frac{V}{W})\delta}{2R_{gas}T}} - e^{-\frac{nF(\frac{V}{W})\delta}{2R_{gas}T}} \right), \quad \text{Eq (16)}$$

where V is the voltage between the archaea and bacteria, W is their distance, n is the number of electrons produced and F is the Faraday constant 96485.33 C mol⁻¹. For a small $(\frac{V}{W})\delta$ value, the flux can be approximated as

$$J_{EF} = k^0 M \cdot MH \left(\frac{nF(\frac{V}{W})\delta}{R_{gas}T} \right) = \alpha \frac{\partial \phi}{\partial x}, \quad \text{Eq (17)}$$

where $\alpha = k^0 M \cdot MH \left(\frac{nF\delta}{R_{gas}T} \right)$, and $\frac{\partial \phi}{\partial x} = \frac{V}{W}$ is the potential gradient or electric field E .

Thus, electron hopping on conductive pili or matrix driven by an electric field yields

$$\phi \frac{\partial MH}{\partial t} = \phi \nabla \cdot J_{EF} + \phi R_r \quad \text{Eq (18)}$$

Assuming that the electric potential is set by the reaction central to cell metabolism,

$$\phi_A = \phi_A^0 - \frac{R_{gas}T \ln Q_A}{nF} \quad \text{Eq (19)}$$

$$\varphi_B = \varphi_B^o - \frac{R_{gas}T \ln Q_B}{nF} \quad \text{Eq (20)}$$

where φ_A^o and φ_B^o are the standard potential for AOM and SR, respectively, $n = 8$ for electrons transported per reaction (Reaction 1), Q_A and Q_B are the corresponding reaction quotients. Then, the electric field \mathbf{E} is computed from the gradient in the electric potential φ in Eqs. 19 & 20, which in turn then drives electron transport. Such electron hopping driving by an electric field can be expressed as

$$\phi \frac{\partial MH}{\partial t} = \phi R_r + \nabla \cdot (\phi \mathcal{D}_{MH} \nabla MH) + \phi \nabla \cdot \mathbf{J}_{EF} \quad \text{Eq (21)}$$

where R_r the net rate of production and consumption, MH is the extracellular concentration of reduced redox molecules.

2.2. Model implementation

AOM consortia were represented as three-dimensional spheres with aggregate radii up to 25 μm , comparable to observations (Boetius et al. 2000, Dekas et al. 2013, Knittel et al. 2005, McGlynn et al. 2015, Nauhaus et al. 2007, Nauhaus et al. 2002, Orphan et al. 2009). The domain radius, which includes the surroundings of the consortia, was set to 2.5-times of the aggregate radius. In the model, the 3D spherical setting was represented by a circle, imposing rotational symmetry at the vertical axis. The observed distribution of archaea and bacteria in the aggregates varies from highly clustered to interspersed (McGlynn et al. 2015). We thus modeled three distinct arrangements – ‘spherical layers’, in which archaea are surrounded by bacteria, ‘half-half’, consisting half spheres of bacteria and archaea, and two ‘enclosed hemispheres’ of archaea surrounded by bacteria (Fig. S1).

All reaction mechanisms contained CH_4 , HCO_3^- , $\text{CO}_2(\text{aq})$, CO_3^{2-} , SO_4^{2-} , HS^- , H^+ as state variables, with SRB-MIET and HS_2^- -MIET pathways both also including a dissolved intermediate, and DIET containing H_2 and M and MH as described above. At the outer domain boundary, the state variables were set to either fixed concentrations reflecting the environmental conditions, or a no flux condition is imposed (Table 1; Supporting Information Appendix A6). Initial conditions were set to the environmental conditions, or for intermediates to a sufficiently low concentration to allow for methane oxidation to take place within the aggregates. We assume the same cell density and cell-specific volume in all models, with cell numbers varying with aggregate size. All simulations were run to steady state.

Cell-specific rate constants (k_A and k_B) are unknown, and hence simulations were carried out in which they were varied across a wide range (see Table 1). Similarly, simulations for a range of initial ratios of electron donors and acceptors involved in DIET were carried out, varying the values of f_M , f_D . Additionally, simulations with $M_{tot} = 0.01$ and 1 mmol L^{-1} and conductivity (σ) ranging from 10^{-4} to 10^4 S m^{-1} , encompassing the 0.1-10 S m^{-1} determined by Malvankar et al. (2011) and Eaktasang et al. (2016), were performed. The main model parameters are defined in Table S1 (Supplementary Information Appendix A5).

Models were implemented in COMSOL Multiphysics (COMSOL 5.3, COMSOL Inc., Burlington, MA, USA). Postprocessing was carried out in MATLAB 2016b (MathWorks, Natick, MA, USA).

2.3. Statistical analysis

Increasing aggregate size can lead to differences in the distribution of activity within aggregates. In order to investigate whether the spatial variability differs between mechanisms, slopes (and variance) of (relative) activity vs. aggregate radius were calculated for individual aggregates with identical parameterization. For the observational data, slope and variance were computed for 41 archaeal aggregates paired with the specific *Desulfobacteraceae* lineage SEEP-SRB1a (AS) and 21 archaeal aggregates paired with non-SEEP-SRB1a *Deltaproteobacteria* (AD) first, and then combined to represent the variability of activity vs. size for the observational data (McGlynn et al. 2015). Finally, a Student's t-test was performed to assess if the slopes between the three model mechanisms and the observations differed significantly. Values of $p < 0.05$ and $p < 0.01$ were considered significant and highly significant, respectively. The statistical analyses were performed using MATLAB 2016b (MathWorks, Natick, MA, USA).

3. Results and Discussion

In this section we present our model simulations and compare them to observations. First, we examine the feasibility of different syntrophic reaction pathways (SRB-MIET, HS_2 -MIET, and DIET) by comparing modeled to measured AOM rates. Then, the possibility of these pathways is further assessed by comparing the spatial variation of archaeal and bacterial activity with FISH-nanoSIMS data of single-cell anabolic activity, across a range of aggregate radii and spatial arrangements of archaeal and bacterial cells in a consortium. Finally, we explore the variables that control the AOM rate and activity patterns in DIET pathway.

3.1. Comparison of model simulations to measured sediment AOM rates

We first estimated cell-specific AOM rates from data from Hydrate Ridge to compare model results to environmentally relevant dynamics. To that end, cell-specific rates were calculated from measured AOM rates per volume of sediment, combined with reported cell densities. We used Boetius et al. (2000) reported cell densities of 9×10^7 consortia per gram dry sediment (gds) with each consortium containing ≈ 100 ANME-2 cells, corresponding to 9×10^9 ANME cells gds^{-1} . The consortia number and aggregate radius sampled during a subsequent cruise to the same area in August 2000 at the crest of the southern Hydrate Ridge ($44^\circ 34' \text{ N}$, $125^\circ 09' \text{ W}$; 780 m water depth) yielded similar values (Nauhaus et al. 2002, 2005, 2007; Holler et al. 2009). Nauhaus et al. (2005) reported an AOM rate of $2.5 \pm 0.3 \mu\text{mol gds}^{-1} \text{ d}^{-1}$, derived from measured sulfide accumulation and assuming a 1:1 ratio of methane oxidized to sulfate reduced, which results in a cell-specific rate of $0.28 \pm 0.03 \text{ fmol cell}^{-1} \text{ d}^{-1}$, consistent with the estimate of Niemann et al. (2005), who also estimated cell-specific rates of 0.13-0.21 $\text{fmol cell}^{-1} \text{ d}^{-1}$ for the sediment samples from the Hydrate Ridge (ANME-2) based on studies by Boetius et al. (2000) and Treude et al. (2003).

The $0.34 \pm 0.15 \mu\text{mol gds}^{-1} \text{d}^{-1}$ rate of AOM reported by Wegener and Boetius (2009) from the RV Sonne cruise SO165-2 in 2002, translate into a cell-specific rate of $3.8 \pm 1.7 \times 10^{-2} \text{fmol cell}^{-1} \text{d}^{-1}$. Treude et al. (2003) reported 1.27×10^8 aggregates cm^{-3} and a slurry density of 0.2gds cm^{-3} from Hydrate Ridge, resulting in an aggregate density of $6.35 \times 10^8 \text{gds}^{-1}$. Taking 100 ANME cells per aggregate with the reported AOM rate of $0.58 \mu\text{mol gds}^{-1} \text{d}^{-1}$, this gives a cell density of $6.35 \times 10^{10} \text{cells gds}^{-1}$ and cell-specific AOM rate of $0.01 \text{fmol cell}^{-1} \text{d}^{-1}$. Finally, for a cell density of 9×10^9 ANME cells gds^{-1} , the AOM rates reported in Nauhaus et al. (2002), Nauhaus et al. (2007) and Holler et al. (2009) correspond to 1.7, 25.6, and $33.3 \text{fmol cell}^{-1} \text{d}^{-1}$, respectively.

These cell-specific AOM rates, on the order of 10^{-2} to $10^2 \text{fmol cell}^{-1} \text{d}^{-1}$, were compared to those computed for the three different syntrophic reaction pathways considered. Because several parameters in the kinetic model formulations – most importantly the rate constants for archaeal and bacterial substrate utilization, k_A and k_B , respectively – are *a priori* poorly constrained, they were varied over a wide range to assess the sensitivity of the model (see section 2.1 for the rate expressions; note also that unless specified otherwise, cell-specific rates reported here are consortia averages, to allow for a meaningful comparison across consortia of different sizes). Results from our model simulations suggest that all three modeled pathways can reach the cell-specific rates that approach, match, or even exceed the empirical AOM rate measurements (Fig. S2). But modeled AOM rates were considerably lower for SRB-MIET models (with an upper limit on the order of $3 \times 10^{-2} \text{fmol cell}^{-1} \text{d}^{-1}$). At some point ($k_A \geq 10^{-15} \text{mol cell}^{-1} \text{d}^{-1}$), AOM rates no longer increased with increasing maximum cell-specific rates (k_A, k_B) for SRB-MIET models. This is caused by thermodynamic constraints that arise when diffusion is too slow to prevent local accumulation of reaction products, consistent with our previous findings (Orcutt and Meile 2008). The maximum AOM rate for SRB-MIET of $\sim 10^{-2} \text{fmol cell}^{-1} \text{d}^{-1}$ is achieved for the smallest aggregate considered ($r = 1.5 \mu\text{m}$), consistent with diffusion limiting the removal of reaction products. Simulations of SRB-MIET with parameterizations that yield high methane oxidation rates result in unevenly distributed activity, with only cells close to the archaeal-bacterial border being active. For a given spatial arrangement of archaea and bacteria, smaller aggregates can sustain higher average cell-specific rates of AOM if the reaction mechanism relies on diffusional exchange of metabolites, due to the closer proximity of archaeal and bacterial cells and hence shorter distances between the location of production and consumption of chemical intermediate species. This high rate could also be achieved by distributing partner organisms such that every cell is in close contact with at least on cell of another type.

The thermodynamic constraints on archaeal cells were much more pronounced for the SRB-MIET than the disulfide pathway because the Gibbs free energy of reaction at standard state for the archaea is more negative for the latter mechanism (note the difference in ΔG^0 of reaction 2 ($\Delta G^0 = 14.8 \text{kJ (mol CH}_4\text{)}^{-1}$) and reaction 4 ($\Delta G^0 = -62.6 \text{kJ (mol CH}_4\text{)}^{-1}$). Additionally, the reaction quotient for the HS_2^- -MIET pathway varies with the power of $4/7$ for the reduced product per methane oxidized, while it is

linear for acetate or varies with the power of 4 for H_2 in SRB-MIET, leading to less build-up of HS_2^- (see discussion in Supplementary Information Appendix A3). Our simulation results are consistent with the findings of Sørensen et al. (2001), in which they suggested that intermediate species such as hydrogen, acetate, and methanol are excluded from the possible electron shuttles for AOM consortia due to thermodynamic and kinetic constraints. Thus, in the absence of mechanisms that enhance exchange beyond molecular diffusion in a three-dimensional arrangement of bacterial and archaeal cells, SRB-MIET does not seem to be able to support commonly observed rates of AOM.

3.2. Comparison of simulations to intra-aggregate activity observations

Models that yield AOM rates between 0.01 and 100 fmol cell⁻¹ d⁻¹, broadly consistent with field observations, were investigated further. We compared the outcome of these simulations with measurements from McGlynn et al. (2015), where anabolic activity was calculated for single cells, extracted from co-registered fluorescence *in situ* hybridization and nanoscale secondary ion mass spectrometry (FISH-nanoSIMS) combined with ¹⁵N stable isotope probing. It was assumed that in the experiments of McGlynn et al. (2015) the spatial distribution of N assimilation is proportional to the metabolic rates, and that the ¹⁵N incorporation reflects the activity associated with methane oxidation. For a growth yield Y_{CH_4} of 0.6 g cell dry weight per mol CH_4 oxidized (Nauhaus et al. 2007), a specific growth rate of $\mu_{cell} = 0.0068$ d⁻¹ (McGlynn et al. 2015), and a biomass density ρ of 4.8×10^5 g cell dry weight m⁻³ (McGlynn et al. 2015), the catabolic AOM rate ($=\mu_{cell} \cdot \rho / Y_{CH_4}$) is 1.5 fmol cell⁻¹ d⁻¹. This falls well within the range of cell-specific environmental AOM rates, suggesting that the patterns of activity that have been observed by McGlynn et al. (2015) are comparable to those occurring under environmentally relevant conditions.

McGlynn et al. (2015) showed that the average cell-specific N uptake does not vary significantly with aggregate radius (n = 62; slope = 0.02 and 0.006 for archaeal and bacterial cells, respectively; see Supporting Information Appendix A7 Fig. S4 A&B). Simulations for the SRB-MIET pathway yielded AOM rate distributions that differ from the observed ¹⁵N assimilation patterns. Average cell-specific AOM rates for the SRB-MIET pathway significantly decrease when increasing the aggregate radius (Fig. 2). When the archaea and bacteria are spatially separated within a consortium, AOM by the SRB-MIET pathway becomes energetically less favorable as the aggregate radius increases and diffusion of intermediate species (e.g., H_2 , acetate) becomes limiting. As a consequence, the concentration of the product of methane oxidation (e.g., acetate or H_2) builds up, ultimately making the reaction energetically less favorable. In contrast, the HS_2^- -MIET pathway mediated by a sulfate-reducing methanotrophic archaeon shows AOM rate distributions that are comparable with the observed ¹⁵N assimilation patterns. This difference between SRB-MIET and HS_2^- -MIET reflects that archaea are less thermodynamically challenged in the HS_2^- -MIET pathway. Similar to the model predictions for HS_2^- -MIET, AOM rate distribution patterns for the hypothesized DIET pathway are also consistent with the experimental nanoSIMS data from McGlynn et al. (2015). Even for very large AOM

consortia with a radius of 25 μm , the average cell-specific AOM rates in the model are within a few percent of the rates for a small aggregates with a radius of 1 μm . Both of these models differ substantially from the SRB-MIET model, where cell-specific AOM rates in aggregates of 6 μm radius are only $\sim 10\%$ of those in 1.5 μm sized aggregates (Fig. 2).

In nature, spatial arrangements of archaea and bacteria within an aggregate vary from highly-segregated to well-mixed (Knittel et al. 2005, McGlynn et al. 2015, Orphan et al. 2009). Empirical analyses of cell-specific anabolic activity within AOM consortia in McGlynn et al. (2015) revealed that the spatial arrangement of the archaea and bacteria does not influence the observed activity of the entire consortia and that cell-specific activity for individual archaea and bacteria is unrelated to the proximity to the nearest partner (see Figure 2b in McGlynn et al. 2015 and Fig. S5). These data contrast with the model simulations for the SRB-MIET pathway, where cell-specific rates varied with aggregate size and arrangement (Fig. 2).

The observational data showed that cell-specific anabolic activity (^{15}N incorporation) is rather uniformly distributed within an aggregate, regardless of the AOM consortium radius or the segregation of archaea and bacteria (see Supporting Information Appendix A7 Figs. S4 C&D and S5 C&D). For SRB-MIET, intra-aggregate variability of cell-specific rates of both archaea and bacteria is more pronounced, and grows as aggregate radius or the segregation of archaea and bacteria increases (Fig. 3 A&D). Variability was lower at low AOM rates, and while the spatial variation in bacterial activity can approach the observed ones (in small aggregates at rates on the order of $\sim 3 \times 10^{-2}$ $\text{fmol cell}^{-1} \text{d}^{-1}$), the modeled spatial variability in archaeal activities clearly exceeded the observed values, even for the smallest aggregates, independent of arrangement (Fig. 3 A). In contrast, DIET and HS_2 -MIET model simulations showed little to no trend of the intra-aggregate variation in archaeal cell-specific rates with aggregate size (Fig. 3 B&C), for all arrangements. The slight variation seen in the experimental data (see Supporting Information Appendix A7 Figs. S4 C&D and S5 C&D) were not observed in DIET and HS_2 -MIET model simulations, which we tentatively attribute to the fact that model simulations only reflect variations in a limited set of substrates, but do not reflect other factors that may be biologically relevant to AOM consortia activity in situ including, e.g., trace nutrients (Glass and Orphan 2012). However, DIET and HS_2 -MIET model simulations showed some spatial intra-aggregate variation in bacterial cell-specific rates, which increases with aggregate size, separation between archaeal and bacterial cells, and an increase in k_B (Fig. 3 E&F).

The modeled spatial variability in bacterial activity depends on the relative kinetics of bacterial and archaeal metabolism. In simulations with bacterial kinetics being fast compared to the archaea (e.g., $k_B = 10^{-10}$ $\text{m}^3 \text{cell}^{-1} \text{d}^{-1}$, compared to $k_A = 10^{-14}$ $\text{mol cell}^{-1} \text{d}^{-1}$, which corresponds to $k_B \sim 10^{-14}$ $\text{m}^3 \text{cell}^{-1} \text{d}^{-1}$ for HS_2 -MIET; see Eqs. 9&10), all pathways showed an increase in the spatial variability of the bacterial cellular activity with increasing aggregate size (Fig. 3 D-F). At lower values of k_B , however, the cell-specific rates of the bacteria varied less for all modeled pathways, consistent

with rather homogeneous activity distribution observed by McGlynn et al. (2015). For both MIET pathways (SRB-MIET and HS₂-MIET), lower bacterial rate constants led to higher substrate levels in the surroundings of the aggregates (see e.g. Supporting Information Appendix A7 Fig. S6). We also observed a slight decrease of the spatial variability of the archaeal cellular activity at faster bacterial kinetics k_B (Fig. 3A), as a result of faster scavenging of methane oxidation products by bacterial cells. Such fast scavenging process by bacteria leads to a strong substrate gradient that is favorable for archaea, but unfavorable for bacteria.

The combined macro- and micro-scale observations provide constraints on the microbial kinetics, because the rate of AOM strongly depends on k_A , while the intra-aggregate activity patterns are dependent on the relative magnitude of k_B . This is reflected in the finding that for a fixed value of archaeal cell specific rate constant k_A , the rate of AOM remained relatively constant at the lower bacterial cell specific rate constants (Supporting Information Appendix A7 Fig. S7), and then increased when k_B reached a certain value for models with SRB-MIET pathway. Faster k_B allowed depletion of electron exchange carriers produced by the archaea, preventing the build-up of products. This pattern held until a point was reached in which spatial gradient of exchanging chemical concentration becomes too large to sustain the bacterial reactions (not shown). For models simulating the DIET pathway, the rate of AOM slightly increased with an increase in k_B and then reached a maximum rate (Supporting Information Appendix A7 Fig. S7), reflecting that in our implementation, the rates of AOM and SR depend on M and MH (Eqns. 11 and 12). As the HS₂⁻ concentration reached in our simulations had a negligible impact on the energetics, the rate of AOM did not vary with k_B in the HS₂⁻-MIET simulations.

3.3. Controls on the rate of AOM by direct interspecies electron transport

At environmentally relevant rates of AOM, patterns in rates and intra-aggregate activity distributions across different aggregate sizes and archaeal-bacterial spatial arrangements are consistent with results from both DIET and HS₂-MIET simulations. However, recent genomic and microscopy evidence suggests DIET is taking place in these aggregates. For instance, metagenomic and transcriptomic analyses of ANME-1 dominated sample by Meyerdierks et al. (2010) observed clustered genes annotated as secreted multi-heme c-type cytochromes that were expressed leading the authors to hypothesize that direct electron transfer may be a possible mode for the syntrophic association between ANME and their sulfate-reducing bacterial partner. More recently, McGlynn et al. (2015) and Wegener et al. (2015) provided further genomic, microscopy, and physiological evidence supporting the possibility of DIET as a syntrophic mechanism within various phylogenetic groups of methane-oxidizing ANME in partnership with sulfate-reducing bacteria. Below we explore factors that may control DIET, and assess the impact of process descriptions and parameters that are currently poorly constrained by observational data.

3.3.1. Rate expressions and acid-base dynamics

The kinetic rate expressions used to describe syntrophic AOM reflect general controlling factors, but have not yet been established experimentally. To assess the effect of alternative rate laws, simulations in which the rate of AOM is independent of the concentration of the redox-active molecules fixed on conductive pili or matrix are compared to simulations that are dependent on M (oxidized) and MH (reduced; see Eqns. 11 and 12). Upon adjusting the values of k_A and k_B , our model simulations reveal the same increasing pattern in AOM rate (R_A) with increasing k_A and k_B (Fig. 4). Such increasing rates of AOM with increasing k_A and k_B were found for SR rate expressions linearly depending on H_2 , or independent of H_2 (Eq. 12).

We also tested the impact of intra-aggregate pH variation on AOM and model performance (see Supporting Information Appendix A5 for the calculation of pH). Simulations showed negligible difference between simulated pH and fixed pH models at small aggregate radii (1.5 μm - 12.5 μm) for simulated AOM rates less than ~ 10 $\text{fmol cell}^{-1} \text{d}^{-1}$. However, at a larger aggregate radius (25 μm) and rates greater than 10 $\text{fmol cell}^{-1} \text{d}^{-1}$, AOM rates with fixed pH simulations but otherwise identical parameterization were slightly higher than those of models with dynamic pH. For instance, with k_A and k_B at $10^{-11} \text{m}^3 \text{cell}^{-1} \text{d}^{-1}$, modeled AOM rates with fixed pH exceeded the ones with pH simulated by approx. 10% for aggregates with $r = 25$ μm . Thus, our simulations suggest that intra-aggregate pH variations are unlikely the main control on AOM rates. The modeled pH remained similar to the imposed seawater value of 8.2, indicating that protons produced in the oxidation of methane (Reaction 6) are efficiently buffered at environmentally relevant rates. However, in direct extracellular electron transfer, the transfer of electron can be much faster than proton diffusion, which can lead to pH gradients (Korth et al. 2015, Franks et al. 2009). Our modeled DIET simulations showed the establishment of such pH gradients, however these gradients only occurred at rates exceeding values reported from methane seep environments ($> 10^3 \text{fmol cell}^{-1} \text{d}^{-1}$) at large aggregate size (25 μm). Our additional simulations with artificially accelerated proton diffusion allowed for higher rates, indicating the potential role of pH variations to limit AOM at high rates and large aggregate size. We note that in addition to the modeled thermodynamic impact here, a decrease in pH at higher AOM rates may also impede proton transport across outer cell membranes, impacting extracellular electron transport as documented by Okamoto et al. (2017) for *Shewanella oneidensis* MR-1.

3.3.2. Electron transport

The nature and description of electron transport between archaea and bacterial partners is a critical issue in AOM aggregates. Described in detail in section 2.1.3, we here explore the impact of several key factors that determine the electron transport rate and cell-specific activities.

Concentration of redox molecules in cell-to-cell electron transport

The transport coefficient for redox-active molecules (reduced: MH; oxidized: M) located on conductive pili or matrix was estimated to be on the order of $10^{-7} \text{m}^2 \text{s}^{-1}$ (see Eq. 14 below, with $M_{tot} = 0.01 \text{mmol L}^{-1}$; $k^0 = 10^4 \text{m}^4 \text{mol}^{-1} \text{s}^{-1}$, $\delta = 0.7 \text{nm}$),

comparable to a value reported for a conductive filament network (charge diffusion coefficient of $3.5 \times 10^{-7} \text{ m}^2 \text{ s}^{-1}$; Meysman et al. 2015). This exceeds chemical diffusion by several orders of magnitude. Here, the concentration of redox molecules was varied across a range of 0.01-1 mmol L^{-1} to explore its impact on electron transport in our models. With the increase of M_{tot} , AOM rates increased linearly, as shown in Fig. 5 A. This is qualitatively consistent with the findings reported by Storck et al. (2016), who showed that a 10-fold decrease of the amount of conductive pili or matrix (N_{nw}) from 100 to 10 per cell pair lead to 60% decrease of electron transport rate. The amount of conductive pili or matrix (N_{nw}) is directly related to the total redox molecule concentration (M_{tot}). However, simulations in which the reaction kinetics were independent of M and MH showed little impact of an increase in M_{tot} (and hence transport coefficient) on AOM, indicating that in our model, AOM is limited by the reaction, rather than electron transport processes. For instance, in model simulations with kinetic rate expressions independent of M and MH, the AOM rate remained constant when M_{tot} increases from 0.01 to 1 mmol L^{-1} (k_A and k_B at $10^{15} \text{ mol cell}^{-1} \text{ d}^{-1}$, aggregate radius $r = 25 \text{ }\mu\text{m}$).

Electrical field as an additional driving force

Electron transport can be driven by a concentration gradient in electron carriers (M and MH) or an electric field (Strycharz-Glaven et al. 2011). Considering the electrical field as a driving force for electron transport in addition to the gradient in oxidized cytochromes did not significantly impact on AOM rates (Fig. 4). Furthermore, there was no significant difference between simulations with electric field as sole driving force and simulations with redox gradient as driving force (not shown). This finding that electron transport between archaea and bacteria is not limiting is also supported by results showing that increasing electron transfer rate constant (k^0) had little impact on AOM rate for $k^0 > 10^2 \text{ m}^4 \text{ mol}^{-1} \text{ s}^{-1}$, corresponding to a transport coefficient of $>10^{-9} \text{ m}^2 \text{ s}^{-1}$. However, the simulated AOM rate significantly decreased at $k^0 \leq 10^2 \text{ m}^4 \text{ mol}^{-1} \text{ s}^{-1}$ (Fig. 5 B). Noticeably, the variation of intra-aggregate archaeal and bacterial activity also began to significantly increase and differ from observations at $k^0 < 10^2 \text{ m}^4 \text{ mol}^{-1} \text{ s}^{-1}$ (Supporting Information Appendix A7 Fig. S8). Storck et al. (2016) reported that doubling the electron transfer rate constant leads to a doubling of electron transfer rate, also implying a doubling of the oxidation rate. Our model simulations suggest that the finding from Storck et al. (2016) remains true at small k^0 ($\leq 10^2 \text{ m}^4 \text{ mol}^{-1} \text{ s}^{-1}$). Overall, the electron transfer rate constant is a critical factor controlling electron transfer by impacting the effective diffusion coefficient (D_{MH}) of redox-active molecule (M and MH).

Voltage loss

Voltage losses can negatively affect transport efficiency in DIET, and ohmic losses (η_{res}) and activation losses (η_{act}) have been suggested to be dominant factors (Storck et al. 2016). Ohmic losses (η_{res}) and activation losses (η_{act}) were calculated using the Ohm's law and Butler-Volmer equation, respectively. Here we investigated the importance of these two voltage loss terms and compare them to the voltage available from the AOM reaction (Eq. 19).

Ohmic loss (η_{res}) is a result of electronic resistance and has been explored in some recent studies (Malvankar et al. 2011, 2014; El-Naggar et al. 2010). It can be calculated as (Storck et al. 2016)

$$\eta_{res} = \rho_{nw} \cdot L_{nw} \cdot I / (N_{nw} \cdot N_{ANME} \cdot A_{nw}), \quad \text{Eq (22)}$$

where ρ_{nw} is the electrical resistivity of a pilus, L_{nw} is the length of a single pilus, A_{nw} is the cross-sectional area of a single pilus, N_{nw} is the number of conductive pili per cell, I is the current generated as a result of methane oxidation and can be estimated as $I = R_{AOM} \cdot N_{ANME} \cdot n \cdot F$, where R_{AOM} is the methane oxidation rate, N_{ANME} is the number of archaeal cells and n the electrons transferred per reaction. We take conductive pili as an example to illustrate the factors that control voltage losses in DIET. With an electrical resistivity of a pilus (ρ_{nw}) of $1 \Omega \cdot m$ (Storck et al. 2016), a cross-sectional area of a single pilus (A_{nw}) of $1.26 \times 10^{-17} \text{ m}^2$ (Storck et al. 2016), length of a single pilus L_{nw} on the order of the aggregate size (10^{-6} m), a current I of $7 \times 10^{-13} \text{ A}$ (at $R_{AOM} = 10 \text{ fmol cell}^{-1} \text{ d}^{-1}$) and 10 conductive pili (N_{nw}) per cell, η_{res} is $7 \times 10^{-5} \text{ V}$. This is substantially smaller than the AOM potential obtained from our model simulations, which is on the order of 10^{-2} V , and suggests that ohmic loss is not a determining factor in our current model.

Activation loss (η_{act}) is another factor that may influence DIET electron transport, accounting for the voltage losses when an electron is transferred from the cell to the conductive pili or vice versa, due to the activation energy needed for a redox reaction. According to Storck et al. (2016) and Strycharz-Glaven et al. (2011), the redox activation losses can be approximated as

$$\eta_{act} = \frac{I \cdot R_{gas} \cdot T \cdot L_{nw}}{N_{nw} N_{ANME} \delta n^2 F^2 A_{act} k^0 \left(\frac{M_{tot}}{2}\right)^2} \text{ when } \delta \cdot \eta_{act} / W < 0.05, \quad \text{Eq (23)}$$

where I is the current generated as a result of methane oxidation and is the same as described in the equation for ohmic loss (η_{res}), L_{nw} is the length of a single pilus, R_{gas} is the universal gas constant ($8.314 \text{ J K}^{-1} \text{ mol}^{-1}$), T is the temperature in K, N_{nw} is the number of conductive pili per cell, N_{ANME} is the number of archaeal cells, δ is the redox molecules spacing width, n the electrons transferred per reaction, F is the Faraday constant $96485.33 \text{ C mol}^{-1}$, A_{act} is the redox activation area per cell (equivalent to 10% of cell surface area), k^0 is the electron transport rate constant, and M_{tot} is the total concentration ($=M+MH$) (Storck et al. 2016). With the same parameters and the current I estimated above, the maximum η_{act} can be estimated to be $1 \times 10^{-7} \text{ V}$ at $M_{tot} = 0.01 \text{ mmol L}^{-1}$ and $k^0 = 10^4 \text{ m}^4 \text{ mol}^{-1} \text{ s}^{-1}$, which is negligible. In contrast, a value of $k^0 = 1 \text{ m}^4 \text{ mol}^{-1} \text{ s}^{-1}$, a decrease by a factor of 10^4 from the default k^0 discussed above would result in an activation loss at an order of $1 \times 10^{-3} \text{ V}$, suggesting activation loss becomes the dominating factor for voltage loss. This is consistent with the findings reported by Storck et al. (2016).

Coupling strength between electron production and conduction

To test how electron transport via the diffusion of dissolved electron carriers ($DH = H_2$ in our model) and conduction of pili or matrix may impact AOM, the fraction of electrons transported via conductive pili or matrix was varied. This was implemented as factors f_M and f_D in reactions 6 & 7, where higher values of f_M imply

lower production of the reduced electron pool molecules *DH*. Simulations suggested that higher loading percentage onto conductive pili or matrix leads to higher AOM rate in general (Fig. 5 C). AOM rates drastically declined at electron conduction coupling strengths (% , defined as $f_M/8 \times 100$, Reaction 6) below 50%. At coupling strength of less than 50%, AOM rates differed between simulations with different spatial arrangements. It is also noted that the variation of archaeal activity significantly ($p < 0.05$) increases at lower coupling strengths (<40%, see Supporting Information Appendix A7 Fig. S9A). The declining AOM rates and increasing intra-aggregate activity variation are due to the increasing thermodynamic constraints resulting from the build-up of H_2 , which increases the reaction quotient,

$$Q_{R6} = \prod a_i^{v_j} = \frac{a_{HCO_3} a_H a_{H_2}^{f_D} a_{MH}^{f_M}}{a_{CH_4} a_M^{f_M}},$$

and subsequently increases ΔG and decreases F_T to the point where F_T for reaction R6 (Eq. 4) becomes 0. Our simulations indicated that under baseline parameterization electron transport of at least 50% by conduction gives AOM rates and intra-aggregate activity spatial variation pattern consistent with observations.

A decrease in AOM rates was observed when incubating ANME-1 consortia with H_2 and methane (Wegener et al. 2015), when considering H_2 as the potential dissolved electron carriers (D and DH). This might be due to electron transport being limited by diffusion of DH (here H_2), possibly in combination with syntrophic decoupling. Once electrons are loaded onto conductive pili or matrix over a certain percentage ($\geq 50\%$), electron transfer does not limit AOM. At a slow effective diffusion of redox molecules with small electron transfer rate constant, AOM rates would have a higher dependency on the activation loss and resistance loss on conductive pili or matrix.

3.4. Metabolic coupling in syntrophic communities

The results of our 3D modeling simulations suggest good agreement between measurements (aggregate AOM rates and spatial activity patterns) and the DIET models. The comparison with cell-specific data from McGlynn et al. (2015) help constrain parameters such as k_A , k_B , M_{tot} , k^0 and f_M . Thus, the models developed here serve as predictive tools for assessing potential syntrophic relationships and major parameters that may influence sulfate-coupled AOM *in situ*. For example, if future measurements of AOM consortia yielded lower cell-specific AOM rates ($< 10^{-3}$ fmol cell⁻¹ d⁻¹) then the diffusion controlled SRB-MIET could be a possible mechanism for small aggregates ($\leq 6 \mu m$). Yet it should be noted that the models presented here are not exhaustive for the range of metabolic possibilities. For example, we have not considered the potential for metabolic switching behavior (Steunou et al. 2006). Our modeling efforts could also be adapted and applied to AOM consortia using other terminal electron acceptors, including nitrate (Haroon et al. 2013; Raghoebarsing et al. 2006) and metal oxides (Beal et al. 2009; Scheller et al. 2016). Ultimately the broad-scale mechanisms modeled here will need to be connected to more detailed perspectives of the entire physiology and metabolism of the cell, as for example informed by genome-enabled metabolic models. It is important to also stress that activation and ohmic losses are largely dependent on electron transport distance

and abundance of conductive pili or matrix (here expressed by L_{nw} and N_{nw}). These are likely to vary spatially within an aggregate (Reguera et al. 2006, Wegener et al. 2015), and thus require further observational studies that constrain these and other characteristics that impact electron conduction.

Finally, it is noteworthy that not only do the small-scale observations help differentiate between mechanisms, but the combination of environmental rate estimates with intra-aggregate activity distribution helps constrain rate constants. Specifically, we find that k_A is well constrained by cell specific AOM rates and is on the order of $>10^{-15} \text{ m}^3 \text{ cell}^{-1} \text{ d}^{-1}$ for DIET and $>10^{-17} \text{ mol cell}^{-1} \text{ d}^{-1}$ for MIET pathways; k_B is no more than 100-fold larger than k_A to be consistent with the observed intra-aggregate activity patterns (Fig. 3 D-F). The product of M_{tot} and k^0 determines the effective diffusion coefficient D_{MH} , which has to exceed $10^{-9} \text{ m}^2 \text{ s}^{-1}$ to be consistent with observations (compare, e.g., the simulated variation in activity in Fig. S8, where k^0 has to exceed $10^2 \text{ m}^4 \text{ mol}^{-1} \text{ s}^{-1}$ at $M_{tot} = 0.01 \text{ mmol L}^{-1}$, $\delta=0.7 \text{ nm}$ with the observed variability shown in Figs. S4 C&D and S5 C&D; and the variation of AOM rates with aggregate size and cell arrangement shown in Fig. 2 and the corresponding ^{15}N assimilation in Figs. S4 A and S5 A). f_M determines the fraction of electron transport via conduction (see reactions 6&7) and is constrained to give electron conduction coupling strengths greater than 50% in order to be consistent with observed patterns in AOM rates with regard to aggregate size and arrangement, as well as intra-aggregate activity. This connection between micro- and macro-scale observations can help us better understand the response of those microbial organisms to a small-scale environmental disturbance and ultimately how such changes would lead to large-scale variation.

4. Conclusion

We presented reactive transport models describing electron transfer within sulfate reduction-coupled AOM consortia of archaeal and bacterial cells. Microbial activities were simulated for diverse arrangements of archaeal and bacterial cells and consortium sizes. We excluded SRB-MIET as a viable pathway of electron transport in these consortia because the simulated microbial activities are unevenly distributed within each consortium and are limited by the build-up of metabolites. These predictions are inconsistent with experimental observations. Instead our models support DIET as a viable mechanism for extracellular electron transfer within sulfate-coupled AOM consortia. Our proposed DIET model yielded cell specific rates and archaeal activity distributions that were consistent with empirical observations, with little impact of the spatial distribution of bacterial and archaeal cells and consortium sizes. These modeling efforts can be used to guide further empirical and theoretical explorations into the identity and kinetics of extracellular redox-active components within AOM consortia with important environmental roles.

Acknowledgements

This work was supported by the Genomic Sciences Program in the DOE Office of Science, Biological and Environmental Research DE-SC0016469. The authors declare no conflict of interest.

References

- Alperin, M., and Hoehler, T. (2010) The Ongoing Mystery of Sea-Floor Methane. *Science* **329**: 288-289.
- Alperin, M.J., and Hoehler, T.M. (2009) Anaerobic methane oxidation by archaea/sulfate-reducing bacteria aggregates: 2. Isotopic constraints. *Am J Sci* **309**: 869-957.
- Aoki, M., Ehara, M., Saito, Y., Yoshioka, H., Miyazaki, M., Saito, Y., Miyashita, A., Kawakami, S., Yamaguchi, T., Ohashi, A. and Nunoura, T. (2014) A long-term cultivation of an anaerobic methane-oxidizing microbial community from deep-sea methane-seep sediment using a continuous-flow bioreactor. *PLoS One* **9**: e105356.
- Bar-Or, I., Elvert, M., Eckert, W., Kushmaro, A., Vigderovich, H., Zhu, Q., Ben-Dov, E. and Sivan, O. (2017) Iron-coupled anaerobic oxidation of methane performed by a mixed bacterial-archaeal community based on poorly reactive minerals. *Environ Sci Technol* **51**:12293-12301.
- Beal E.J., House C.H., and Orphan V.J. (2009) Manganese- and iron-dependent marine methane oxidation. *Science* **325**:184–187.
- Beyenal, H., Chen, S.N. and Lewandowski, Z. (2003) The double substrate growth kinetics of *Pseudomonas aeruginosa*. *Enzyme Microb Technol*, **32**: 92-98.
- Boetius, A., Ravensschlag, K., Schubert, C.J., Rickert, D., Widdel, F., Gieseke, A., *et al.* (2000) A marine microbial consortium apparently mediating anaerobic oxidation of methane. *Nature* **407**: 623–626.
- Burgess, I., Seivewright, B., and Lennox, R. B. (2006) Electric field driven protonation/deprotonation of self-assembled monolayers of acid-terminated thiols. *Langmuir*, **22(9)**: 4420–4428.
- Chen, Y., Li, Y.-L., Zhou, G.-T., Li, H., Lin, Y.-T., Xiao, X., and Wang, F.-P. (2014) Biomineralization mediated by anaerobic methane-consuming cell consortia. *Sci Rep* **4**: 5696.
- Cherif, M. and Loreau, M. (2010) Towards a more biologically realistic use of Droop's equations to model growth under multiple nutrient limitation. *Oikos*, **119**: 897-907.
- Dekas, A.E., Chadwick, G.L., Bowles, M.W., Joye, S.B., and Orphan, V.J. (2013) Spatial distribution of nitrogen fixation in methane seep sediment and the role of the ANME archaea. *Environ Microbiol* **16**: 3012–3029.
- Dolfing, J. (1992) The energetic consequences of hydrogen gradients in methanogenic ecosystems. *FEMS Microbiol Ecology* **101**: 183-187.
- Eaktasang, N., Kang, C.S., Lim, H., Kwean, O.S., Cho, S., Kim, Y., and Kim, H.S. (2016) Production of electrically-conductive nanoscale filaments by sulfate-reducing bacteria in the microbial fuel cell. *Bioresour Technol* **210**: 61-67.

- El-Naggar, M.Y., Gorby, Y.A., Xia, W., and Nealson, K.H. (2008) The molecular density of states in bacterial nanowires. *Biophys J* **95**: L10-L12.
- El-Naggar, M.Y., Wanger, G., Leung, K.M., Yuzvinsky, T.D., Southam, G., Yang, J., Lau, W.M., Nealson, K.H., and Gorby, Y.A. (2010) Electrical transport along bacterial nanowires from *Shewanella oneidensis* MR-1. *PNAS* **107**: 18127-18131.
- Forster, P., Ramaswamy, V., Artaxo, P., Berntsen, T., Betts, R., Fahey, D.W., *et al.* (2007) Chapter 2: Changes in Atmospheric Constituents and in Radiative Forcing. In Contribution of Working Group I to the Fourth Assessment Report of the Intergovernmental Panel on Climate Change. Solomon, S., Qin, D., Manning, M., Chen, Z., Marquis, M., Averyt, K.B., Tignor, M. and Miller H.L. (eds). Cambridge, United Kingdom and New York, NY, USA: Cambridge University Press, pp. 130-234.
- Franks, A.E., Nevin, K.P., Jia, H., Izallalen, M., Woodard, T.L. and Lovley, D.R. (2009) Novel strategy for three-dimensional real-time imaging of microbial fuel cell communities: monitoring the inhibitory effects of proton accumulation within the anode biofilm. *Energy Environ Sci* **2**:113-119.
- Glass, J. and Orphan, V.J. (2012) Trace metal requirements for microbial enzymes involved in the production and consumption of methane and nitrous oxide. *Front Microbiol* **3**: 61.
- Gonzo, E.E., Wuertz, S. and Rajal, V.B. (2014) The continuum heterogeneous biofilm model with multiple limiting substrate Monod kinetics. *Biotechnol Bioeng*, **111**: 2252-2264.
- Gupta, N., Gattrell, M., and MacDougall, B. (2006) Calculation for the cathode surface concentrations in the electrochemical reduction of CO₂ in KHCO₃ solutions. *J Appl Electrochem* **36**: 161-172.
- Haroon, M.F., Hu, S., Shi, Y., Imelfort, M., Keller, J., Hugenholtz, P., Yuan, Z. and Tyson, G.W. (2013) Anaerobic oxidation of methane coupled to nitrate reduction in a novel archaeal lineage. *Nature* **500**: 567-570.
- Hinrichs, K.U., Hayes, J.M., Sylva, S.P., Brewer, P.G., and DeLong, E.F. (1999) Methane-consuming Archaeobacteria in marine sediments. *Nature* **398**: 802-805.
- Hocking, W.P., Roalkvam, I., Magnussen, C., Stokke, R., and Steen, I.H. (2015) Assessment of the carbon monoxide metabolism of the hyperthermophilic sulfate-reducing archaeon *Archaeoglobus fulgidus* VC-16 by comparative transcriptome analyses. *Archaea* **2015**: 235384.
- Hoehler, T.M., Alperin, M.J., Albert, D.B. and Martens, C.S. (1994) Field and laboratory studies of methane oxidation in an anoxic marine sediment: Evidence for a methanogen - sulfate reducer consortium. *Global Biogeochemical Cycles* **8**:451-463.
- Hoehler, T.M., Alperin, M.J., Albert, D.B. and Martens, C.S. (2001) Apparent minimum free energy requirements for methanogenic Archaea and sulfate-reducing bacteria in an anoxic marine sediment. *FEMS Microbiol Ecology* **38**: 33-41.
- Hoehler, T.M., and Jørgensen, B.B. (2013) Microbial life under extreme energy limitation. *Nature Rev Microbiol* **11**: 83-94.
- Holler, T., Wegener, G., Knittel, K., Boetius, A., Brunner, B., Kuypers, M.M., and Widdel, F. (2009) Substantial ¹³C/¹²C and D/H fractionation during anaerobic

- oxidation of methane by marine consortia enriched *in vitro*. *Environ Microbiol Rep*: 370-376.
- Huskinson, B., Marshak, M., Aziz, M.J., and Gordon, R.G. (2015) Small organic molecule based flow battery. U.S. Patent Application, US20150243991 A1.
- Jin, Q., and Bethke, C. (2003) A new rate law describing microbial respiration. *Appl Environ Microbiol* **69**: 2340–2348.
- Jin, Q., and Bethke, C. (2007) The thermodynamics and kinetics of microbial metabolism. *Am J Sci* **307**: 643–677.
- Kaplan, H., Stevenson, K.J., and Hartley, B.S. (1971) Competitive labelling, a method for determining the reactivity of individual groups in proteins. The amino groups of porcine elastase. *Biochem J* **124**: 289-299.
- Kletzin, A., Heimerl, T., Flechsler, J., van Niftrik, L., Rachel, R., and Klingl, A. (2015) Cytochromes c in Archaea: distribution, maturation, cell architecture, and the special case of *Ignicoccus hospitalis*. *Front Microbiol* **6**: 439.
- Knittel, K., Lösekann, T., Boetius, A., Kort, R., and Amann, R. (2005) Diversity and distribution of methanotrophic archaea at cold seeps. *Appl Environ Microbiol* **71**: 467-479.
- Konhauser, K. (2006) Chapter 3. Cell surface reactivity and metal sorption. In Introduction to geomicrobiology. Konhauser, K. (ed): Blckwell Publishing.
- Korth, B., Rosa, L.F., Harnisch, F., and Picioreanu, C. (2015) A framework for modeling electroactive microbial biofilms performing direct electron transfer. *Bioelectrochemistry* **106**: 194-206.
- Krukenberg, V., Riedel, D., Gruber-Vodicka, H.R., Buttigieg, P.L., Tegetmeyer, H.E., Boetius, A., and Wegener, G. (2018) Gene expression and ultrastructure of meso- and thermophilic methanotrophic consortia. *Environ Microbiol* **20**:1651-1666.
- Malvankar, N.S., Tuominen, M.T., and Lovley, D.R. (2012) Lack of cytochrome involvement in long-range electron transport through conductive biofilms and nanowires of *Geobacter sulfurreducens*. *Energy Environ Sci* **5**: 8651–8659.
- Malvankar, N.S., Vargas, M., Nevin, K.P., Franks, A.E., Leang, C., Kim, B.-C., Inoue, K., Mester, T., Covalla, S.F., Johnson, J.P., Rotello, V.M., Mark, T.T., and Lovley, D.R. (2011) Tunable metallic-like conductivity in microbial nanowire networks. *Nat Nanotechnol* **6**: 573-579.
- Malvankar, N.S., Mark, T.T., and Lovley, D.R. (2012) Comment on “On electrical conductivity of microbial nanowires and biofilms” by S. M. Strycharz-Glaven, R. M. Snider, A. Guiseppi-Elie and L. M. Tender, *Energy Environ. Sci.*, 2011, 4, 4366. *Energy Environ Sci* **5**: 6247
- Malvankar, N.S., Yalcin, S.E., Tuominen, M.T., and Lovley, D.R. (2014) Visualization of charge propagation along individual pili proteins using ambient electrostatic force microscopy. *Nat Nanotechnol* **9**: 1012-1017.
- McGlynn, S.E. (2017) Energy metabolism during anaerobic methane oxidation in ANME archaea. *Microbes Environ* **32**:5-13
- McGlynn, S.E., Chadwick, G.L., Kempes, C.P., and Orphan, V.J. (2015) Single cell activity reveals direct electron transfer in methanotrophic consortia. *Nature* **526**: 531-535.

- Meyerdierks, A., Kube, M., Kostadinov, I., Teeling, H., Glöckner, F.O., Reinhardt, R., Amann, R. (2010) Metagenome and mRNA expression analyses of anaerobic methanotrophic archaea of the ANME-1 group. *Environ Microbiol* **12**:422–439.
- Meysman, F.J.R., Risgaard-Petersen, N., Malkin, S.Y., and Nielsen, L.P. (2015) The geochemical fingerprint of microbial long-distance electron transport in the seafloor. *Geochim Cosmochim Acta* **152**: 122–142.
- Michaelis, W., Seifert, R., Nauhaus, K., Treude, T., Thiel, V., Blumenberg, M., Knittel, K., Gieseke, A., Peterknecht, K., Pape, T., Boetius, A., Amann, R., Jørgensen, B.B., Widdel, F., Peckmann, J., Pimenov, N.V., and Gulin, M.B. (2002) Microbial reefs in the black sea fueled by anaerobic oxidation of methane. *Science* **297**:1013-1015
- Milucka, J., Ferdelman, T.G., Polerecky, L., Franzke, D., Wegener, G., Schmid, M., and Kuypers, M.M. (2012) Zero-valent sulphur is a key intermediate in marine methane oxidation. *Nature* **491**: 541-546.
- Moran, J.J., Beal, E.J., Vrentas, J.M., Orphan, V.J., Freeman, K.H., House, C.H. (2008) Methyl sulfides as intermediates in the anaerobic oxidation of methane. *Environ Microbiol* **10**: 162-173
- Nauhaus, K., Albrecht, M., Elvert, M., Boetius, A., and Widdel, F. (2007) In vitro cell growth of marine archaeal-bacterial consortia during anaerobic oxidation of methane with sulfate. *Environ Microbiol* **9**: 187-196.
- Nauhaus, K., Boetius, A., Krüger, M., and Widdel, F. (2002) In vitro demonstration of anaerobic oxidation of methane coupled to sulphate reduction in sediment from a marine gas hydrate area. *Environ Microbiol* **4**: 296–305.
- Nauhaus, K., Treude, T., Boetius, A., and Krüger, M. (2005) Environmental regulation of the anaerobic oxidation of methane: a comparison of ANME-I and ANME-II communities. *Environ Microbiol* **7**: 98-106.
- Niemann, H., Elvert, M., Hovland, M., Orcutt, B., Judd, A., Suck, I., *et al.* (2005) Methane emission and consumption at a North Sea gas seep (Tommeliten area). *Biogeosciences* **2**: 335–351.
- Okamoto, A., Tokunou, Y., Kalathil, S., Hashimoto, K. (2017) Proton transport in the outer-membrane flavocytochrome complex limits the rate of extracellular electron transport. *Angew Chem Int Ed Engl* **56**: 9082–9086.
- Orcutt, B., and Meile, C. (2008) Constraints on mechanisms and rates of anaerobic oxidation of methane by microbial consortia: process-based modeling of ANME-2 archaea and sulfate reducing bacteria interactions. *Biogeosciences* **5**: 1587-1599.
- Ordonez, M.V., Schrott, G.D., Massazza, D.A., and Busalmen, J.P. (2016) The relay network of Geobacter biofilms. *Energy Environ Sci* **9**: 2677-2681.
- Orphan, V.J., Hinrichs, K.U., Ussler, W.I.I.I., Paull, C.K., Taylor, L.T., Sylva, S.P., Hayes, J.M. and DeLong, E.F. (2001) Comparative analysis of methane-oxidizing archaea and sulfate-reducing bacteria in anoxic marine sediments. *Appl Environ Microbiol* **67**:1922-1934.
- Orphan, V.J., House, C.H., Hinrichs, K.U., McKeegan, K.D. and DeLong, E.F. (2002) Multiple archaeal groups mediate methane oxidation in anoxic cold seep sediments. *PNAS* **99**:7663-7668.
- Orphan, V.J., Turk, K.A., Green, A.M., and House, C.H. (2009) Patterns of ¹⁵N assimilation and growth of methanotrophic ANME-2 archaea and sulfate-reducing

- bacteria within structured syntrophic consortia revealed by FISH-SIMS. *Environ Microbiol* **11**: 1777–1791.
- Pänke, O., and Rumberg, B. (1997) Energy and entropy balance of ATP synthesis. *BBA-Bioenergetics* **1322**: 183-194.
- Phoenix, V.R., Martinez, R.E., Konhauser, K.O., and Ferris, F.G. (2002) Characterization and implications of the cell surface reactivity of *Calothrix* sp. strain KC97. *Appl Environ Microbiol* **68**: 4827-4834.
- Raghoebarsing, A.A., Pol, A., van de Pas-Schoonen, K.T., Smolders, A.J., Ettwig, K.F., Rijpstra, W.I., Schouten, S., Damsté, J.S., Op den Camp, H.J., Jetten, M.S., Strous, M. (2006) A microbial consortium couples anaerobic methane oxidation to denitrification. *Nature* **440**: 918-921.
- Reeburgh, W.S. (1976) Methane consumption in Cariaco Trench waters and sediments. *Earth Planet Sci Lett* **28**: 337–344.
- Reeburgh, W.S. (2007) Oceanic methane biogeochemistry. *Chemical Rev* **107**: 486-513.
- Reguera, G., McCarthy, K.D., Mehta, T., Nicoll, J.S., Tuominen, M.T., and Lovley, D.R. (2005) Extracellular electron transfer via microbial nanowires. *Nature* **435**: 1098–1101.
- Reguera, G., Nevin, K. P., Nicoll, J. S., Covalla, S. F., Woodard, T. L., Lovley, D. R. (2006) Biofilm and nanowire production leads to increased current in *Geobacter sulfurreducens* fuel cells. *Appl Environ Microbiol* **72**:7345–7348
- Šalić, A., Faletar, P., and Zelić, B. (2013) NAD⁺ regeneration in a microreactor using permeabilized baker's yeast cells. *Biochem Eng J* **77**: 88-96.
- Scheller, S., Yu, H., Chadwick, G.L., McGlynn, S.E., and Orphan, V.J. (2016) Artificial electron acceptors decouple archaeal methane oxidation from sulfate reduction. *Science* **351**: 703-707.
- Schink, B., and Stam, A.J.M. (2006). Syntrophism among prokaryotes. In: The Prokaryotes. Dworkin M, Falkow S, Rosenberg E, Schleifer K-H, Stackebrandt E (eds). New York: Springer, pp 309–335.
- Schulz, H. D. (2000). Quantification of early diagenesis: dissolved constituents in marine pore water. In Marine Geochemistry. Schulz, H.D. and Zabel, M. (eds). Springer Berlin Heidelberg, pp. 85-128.
- Sørensen, K.B., Finster, K. and Ramsing, N.B. (2001) Thermodynamic and kinetic requirements in anaerobic methane oxidizing consortia exclude hydrogen, acetate, and methanol as possible electron shuttles. *Microbial Ecology* **42**:1-10.
- Steunou, A.S., Bhaya, D., Bateson, M.M., Melendrez, M.C., Ward, D.M., Brecht, E., Peters, J.W., Kühl, M. and Grossman, A.R. (2006) In situ analysis of nitrogen fixation and metabolic switching in unicellular thermophilic cyanobacteria inhabiting hot spring microbial mats. *PNAS*, **103**: 2398-2403.
- Storck, T., Virdis, B., and Batstone, D.J. (2016) Modelling extracellular limitations for mediated versus direct interspecies electron transfer. *The ISME Journal* **10**: 621-631.
- Strycharz-Glaven, S.M., Snider, R.M., Guiseppi-Elie, A., and Tender, L.M. (2011) On the electrical conductivity of microbial nanowires and biofilms. *Energy Environ Sci* **4**: 4366-4379.

- Strycharz-Glaven, S.M., and Tender, L.M. (2012) Reply to the ‘Comment on “On electrical conductivity of microbial nanowires and biofilms”’ by N. S. Malvankar, M. T. Tuominen and D. R. Lovley, *Energy Environ. Sci.*, 2012, 5. *Energy Environ Sci* **5**: 6250
- Timmers, P.H., Welte, C.U., Koehorst, J.J., Plugge, C.M., Jetten, M.S., and Stams, A.J. (2017) Reverse Methanogenesis and respiration in methanotrophic archaea. *Archaea* **2017**: 1654237.
- Tran, Q.H., Uden, G. (1998) Changes in the proton potential and the cellular energetics of *Escherichia coli* during growth by aerobic and anaerobic respiration or by fermentation. *Eur J Biochem* **251**: 538–543.
- Treude, T., Boetius, A., K., K., Wallmann, K., and Jørgensen, B.B. (2003) Anaerobic oxidation of methane above gas hydrates at Hydrate Ridge, NE Pacific Ocean. *Mar Ecol Prog Ser* **264**: 1-14.
- Valencia, D.P., and González., F.J. (2011) Understanding the linear correlation between diffusion coefficient and molecular weight. A model to estimate diffusion coefficients in acetonitrile solutions. *Electrochem Commun* **13**: 129-132.
- Valentine, D.L. and Reeburgh, W.S. (2000) New perspectives on anaerobic methane oxidation. *Environ Microbiol* **2**:477-484
- Viridis, B., Millo, D., Donose, B.C., Lu, Y., Batstone, D.J., and Krömer, J.O. (2016) Analysis of electron transfer dynamics in mixed community electroactive microbial biofilms. *Rsc Adv* **6**: 3650-3660.
- Wallerstein, J., Weininger, U., Khan, M.A.I., Linse, S., and Akke, M. (2015) Site-specific protonation kinetics of acidic side chains in proteins determined by pH-dependent carboxyl ¹³C NMR relaxation. *J Am Chem Soc* **137**: 3093–3101.
- Wegener, G., and Boetius, A. (2009) An experimental study on short-term changes in the anaerobic oxidation of methane in response to varying methane and sulfate fluxes. *Biogeosciences* **6**: 867-876.
- Wegener, G., Krukenberg, V., Riedel, D., Tegetmeyer, H.E., and Boetius, A. (2015) Intercellular wiring enables electron transfer between methanotrophic archaea and bacteria. *Nature* **526**: 587-590.
- Wegener, G., V. Krukenberg, S.E. Ruff, M.Y. Kellermann, and Knittel, K. (2016) Metabolic capabilities of microorganisms involved in and associated with the anaerobic oxidation of methane. *Front Microbiol* **7**:46.
- Zeebe, R.E., and Wolf-Gladrow, D. (2005) Chapter 2. Kinetics. In *CO₂ in Seawater: Equilibrium, Kinetics, Isotopes*. Halpern, D. (ed), San Diego, USA: Elsevier Science.
- Zinn, M., Witholt, B. and Egli, T. (2004) Dual nutrient limited growth: models, experimental observations, and applications. *J Biotechnol* **113**: 263-279.
- Zhou, Y., Fang, C., Fang, Y., and Zhu, F. (2013) Volumetric and transport properties of aqueous NaB(OH)₄ solutions. *Chin J Chem Eng* **21**: 1048-1056.

Tables

Table 1. Parameterization of reactions

Symbol	Value (unit)	Description
$K_m^{CH_4}$, $K_m^{SO_4}$	37 m M, 1m M	Half saturation constant for methane in AOM and SRB, respectively (Orcutt and Meile 2008)
r_{ANM} , r_{SRB}	0.4 μ m , 0.4 μ m	Radius of archaea, bacteria cell, respectively (Knittel et al. 2005, Aoki et al. 2014, Boetius et al. 2000)
k_A , k_B	10^{18} to 10^8	Archaea and bacteria rate constants: mol cell ⁻¹ d ⁻¹ for k_A , k_B in SRB-MIET mol cell ⁻¹ d ⁻¹ for k_A , m ³ cell ⁻¹ d ⁻¹ for k_B in HS ₂ ⁻ -MIET m ³ cell ⁻¹ d ⁻¹ for k_A , k_B in DIET, except for 1 st order reactions with respect to D, DH and M, MH, for which k_B is in m ⁶ cell ⁻¹ mol ⁻¹ d ⁻¹ , and for no dependency on M, MH, for which k_A and k_B are in mol cell ⁻¹ d ⁻¹ .
DIET parameters		
$[M_{tot}]$ J	10^5 - 10^3 M	Concentration of redox molecules (see section 3.3.2). Baseline value: 10^5 M
k^o	1- 10^4 m ⁴ mo l ⁻¹ s ⁻¹	Rate constant of electron transport on conductive pili or matrix. Baseline value: 10^4 m ⁴ mol ⁻¹ s ⁻¹
δ	0.7 nm	Redox molecules spacing width (Malvankar et al. 2012)
σ	10^4 - 10^4 S m ⁻¹	Conductivity of conductive pili or matrix (Malvankar 2011). Baseline value: 0.1 S m ⁻¹

Parameters are set to baseline values if not noted otherwise. Temperature T is set to 281.15K;
 Aqueous diffusion coefficient: $D_{CO_2} = 1.91 \times 10^{-9}$ m² s⁻¹, $D_{H_2} = 6.31 \times 10^{-9}$ m² s⁻¹ (Schulz 2000), $D_{CO_3} = 1.19 \times 10^{-9}$ m² s⁻¹, $D_{H^+} = 6 \times 10^{-9}$ m² s⁻¹, $D_{OH^-} = 5.27 \times 10^{-9}$ m² s⁻¹ (Gupta et al. 2006); $D_{B(OH)_4} = 9.56 \times 10^{-10}$ m² s⁻¹ (Zhou et al. 2013).
 Fixed concentration boundary conditions are imposed for all chemical species at the outer domain boundary except for HS₂⁻ for which a no flux condition is imposed at the outer domain boundary, and for MH, R-COOH, R-NH₂, for which no flux condition is imposed at the aggregate surface. Boundary conditions are set to: 10^{-4} M HS⁻, 10^{-3} M HCO₃⁻, pH=8.2, 10^{-2} M SO₄²⁻, 10^{-3} M CH₄, 10^{-7} mM acetate

